Supramolecular packing dominant photocatalytic oxidation and anticancer performance of PDI

Jun Wang[a], Di Liu[b], Yongfa Zhu[a,*], Shuyun Zhou[c], Shanyue Guan[c,*]

[a] Department of Chemistry, Tsinghua University, Beijing 100084, PR China
[b] China University of Mining and Technology Campus, Beijing, 100083, PR China
[c] Key Laboratory of Photochemical Conversion and Optoelectronic Materials, Technical Institute of Physics and Chemistry, Chinese Academy of Sciences, Beijing, 100190, PR China

ARTICLE INFO

ABSTRACT

The development of organic supramolecular photocatalytic materials requires a deeper understanding of the structure-activity relationship. Herein, the effects of H/J-type stacking on the photocatalytic mechanism and activity of PDI have been investigated. As a face-to-face arrangement, H-aggregates have higher π-electron conjugation and show more semiconductor characteristics, which results in higher carrier separation and migration efficiency under irradiation. Whereas, J-aggregates exhibit more molecular properties due to its low π-electron conjugation caused by head-to-tail stacking mode. As a result, H-aggregated PDI mainly forms super-oxide radicals ($\cdot O_2^-$) and holes (h^+) through electron-transfer (ET). In contrast, J-aggregated PDI mainly generates singlet oxygen species ($^1O_2$) via energy-transfer (EnT). Benefit from the stronger oxidizability of $\cdot O_2^-$ and h^+, H-aggregated PDI shows higher photocatalytic activity for small molecule degradation and oxygen evolution under visible light. Whereas, J-aggregated PDI exhibits potential application in photocatalytic anti-cancer treatment owing to its high $^1O_2$ quantum yields (0.66) under red light radiation. Our findings may provide a guidance for the development of supramolecular organic photocatalytic materials.

1. Introduction

Supramolecular organic photocatalytic materials have received a great deal of attention in recent years due to their outstanding optical and electronic properties [1–12]. Recently, several successful supramolecular photocatalysis systems have been reported to be applied in water splitting, organic pollutants decomposing and photosynthesis [13–17], such as porphyrin (TPP) [3,13,17], diketopyrrolopyrrole (DPP) [14,15], perylene monoimide (PMI) [16,18] and perylenetracarboxylic diimide (PDI) [19–24]. Wasielewski et al. developed a highly efficient light-absorbing and charge-transport chromophores, PMI supramolecular hydrogel scaffold, worked with centre catalyst of nickel (Ni) to produce hydrogen under visible light [16]. By incorporation of ruthenium (Ru) into PDI supramolecular nanofibers, Würthner's group revealed that such photosensitizer/catalyst (PDI/Ru) assemblies were highly stable and photoactive in water oxidation [24]. In these systems, the supramolecular self-assembly of chromophores is considered as light-harvesting and charge-transport media rather than centre catalyst. The main photoenergy conversion process in these supramolecular chromophore is energy-transfer (EnT). However, recent studies show that some supramolecular nanomaterials can produce effective photogenerated carrier separation through electron-transfer (ET) under irradiation [13,19,20,22]. Very recent, we also demonstrated that purely PDI supramolecular nanostructures not only can generate singlet oxygen species ($^1O_2$) via EnT, but also can produce superoxide radicals ($\cdot O_2^-$) and holes (h^+) through ET [19,20]. Therefore, despite great progress has been made for the application of supramolecular organic materials in the field of photocatalysis, the mechanism of photocatalysis in supramolecular organocatalyst remains obscure. The development of organic supramolecular photocatalytic materials has driven an urgent need for the understanding of the effect of molecular packing on photocatalytic mechanism and activity in supramolecular materials.

PDI and its derivatives are regarded as one of best n-type organic semiconductors and have been widely studied because of their excellent optical and thermal stability, excellent optical trapping and carrier transport properties [2,4,25–27]. As a small molecule with rigid π-electron plane, the stacking modes of PDI molecule are mainly H- and J-type aggregates [28–31]. In H-aggregates, molecules primarily stack in a face-to-face arrangement, while J-aggregates form when molecules predominantly stack head-to-tail [17]. Different coupling modes between the chromophores lead to different physical and chemical

---

properties in H- and J-type aggregated PDI supramolecular materials. To date, numerous studies have focused attention on the influence of PDI molecular stacking on its absorption and fluorescence emission [30–33]. However, to the best of our knowledge, the effects of H/J-type stacking structures on the photocatalytic mechanism and activity of PDI supramolecular organic nanomaterials have never been reported. Herein, we investigated the influence of supramolecular stacking structures on the photoenergy transfer mechanism and photocatalytic oxidation/anticancer performance of PDI.

2. Experimental section

2.1. Preparation of H-PDI and J-PDI supramolecular nanostructures

200.0 mL stock solution of H-PDI or J-PDI (5.0 mM) was prepared with addition of 834 μL of TEA. PDI supramolecular nanostructures were formed by adding 27.3 mL 4.0 M HCl (Scheme S2). It was washed thoroughly with distilled water until the pH of washings turned to be neutral. The collected solid was dried in at 60 °C.

2.2. Characterizations

UV–vis spectra of H-PDI and J-PDI were recorded by Hitachi U-3010 UV–vis spectrophotometer. Morphologies and structures of the pre-pared samples were examined by JEM 1200 transmission electron microscopy (TEM) at an accelerating voltage of 100 kV. UV–vis diffuse reflection spectra (DRS) were obtained on a Hitachi U-3010 UV–vis spectrophotometer. $BaSO_4$ was used as the reflectance standard in the experiment. X-ray photoelectron spectroscopy (XPS ULVAC-PHI, Quantera) was used to estimate the VB positions of H-PDI and J-PDI. The charge effect was calibrated using the binding energy of C1s. The confocal fluorescence images were recorded by the Nikon A1R Eclipse Ti confocal laser scanning microscope with the $40 \times$ water-immersion objective, respectively.

The electrochemical and photoelectrochemical were measured on an electrochemical system (CHI-660B, China). The photoelectric responses of the photocatalysts as light on and off were measured at 0.0 V. A standard three electrode cell with ITO or Pt as a working electrode, a platinum disk as a counter electrode, and a standard calomel electrode (SCE) as reference electrode were used in photoelectric studies. 0.1 M Na_2SO_4 was used as the electrolyte solution. Potentials were given with reference to the SCE.

2.3. $^1O_2$ quantum yields measurements via the chemical method

1,3-diphenylisobenzofuran (DPBF) was used as the $^1O_2$-trapping agent, and RB was used as the standard photosensitizer. In the experiments, 50 mL of ethanol solution with DPBF (20 μg/mL) and PDI (10 μg/mL) were stirred in the dark for 15 min to reach the adsorption/desorption equilibrium prior to the test. A xenon lamp (CEL-HXF300E7, Au-Light, Beijing) with 600 nm bandpass filter (± 1 nm) were used as the light source. The optical density was adjusted to be 12 mW/cm^2. To eliminate the inner-filter effect, the absorption maxima of RB and H/J-PDI were adjusted to 1.1 abs. The absorption of DPBF at 410 nm was recorded at various irradiation times to obtain the decay rate of the photosensitizing process. The $^1O_2$ quantum yield of the PDI in ethanol (Φ_{PDI}) was calculated using the following formula:

$$\Phi_{H/J\text{-}PDI} = \Phi_{RB} * K_{H/J\text{-}PDI} * A_{RB}/(K_{RB} * A_{H/J\text{-}PDI})$$

where K_{PDI} and K_{RB} are the decomposition rate constants of DPBF by the H/J-PDI and RB, respectively. $A_{H/J\text{-}PDI}$ and A_{RB} represent the light absorbed by H/J-PDI and RB, respectively, which are determined by integration of the optical absorption bands in the wavelength range 400–700 nm. Φ_{RB} is the $^1O_2$ quantum yields of RB, and $\Phi_{RB} = 0.86$ in ethanol.

2.4. Photocatalytic experiments

The photodegradation reactions were carried out in quartz tube reactor with a 50 mL 5 ppm phenol solution and 25 mg photocatalyst powders. The visible light source was obtained by a 500 W xenon lamp with cutoff filter (> 420 nm). Before irradiation, the suspension solution was first magnetically stirred in dark for 1 h to reach the adsorption-desorption equilibrium. At given time intervals, 2.0 mL solution were sampled and centrifuged to remove the photocatalysts. The concentration of phenol characterized using HPLC (Lumtech) system. Venusil XBP-C18 (250 mm × 4.6 mm i.d., 5 μm) reversed phase column was used.

The photocatalyst powders (50 mg) were dispersed by a magnetic stirrer in 100 mL 0.01M $AgNO_3$(aq) in an online photocatalytic system (PCX50B and Labsolar-6A, Beijing China PerfectLight). The visible light source was obtained by a 300 W xenon arc lamp (CEL-HXF300E7, Au-Light, Beijing) with cutoff filter (> 420 nm). The irradiance was measured to be 146 mW/cm^2 (CEL-NP2000). The amount of evolved oxygen was determined using a gas chromatograph (GC7920, TCD, Ar carrier).

2.5. In vitro cytotoxicity assay

The in vitro cytotoxicity of H-PDI and J-PDI were investigated on the human Hela cells. First of all, Hela cells were incubated in the 25 cm^2 cell-culture flask and then the cells (104 cells/well) were seeded into a 96-well plate by detaching from the flask. Additionally, we incubated the Hela cells with a series doses of H-PDI and J-PDI for 24 h. After further incubation for 24 h, the mixture of CCK-8 and DMEM (1:10) were added to the 96-plate. The cell viability was calculated as the ratio of the absorbance of the wells. The absorbance at 450 nm was measured by Thermo Multiskan FC.
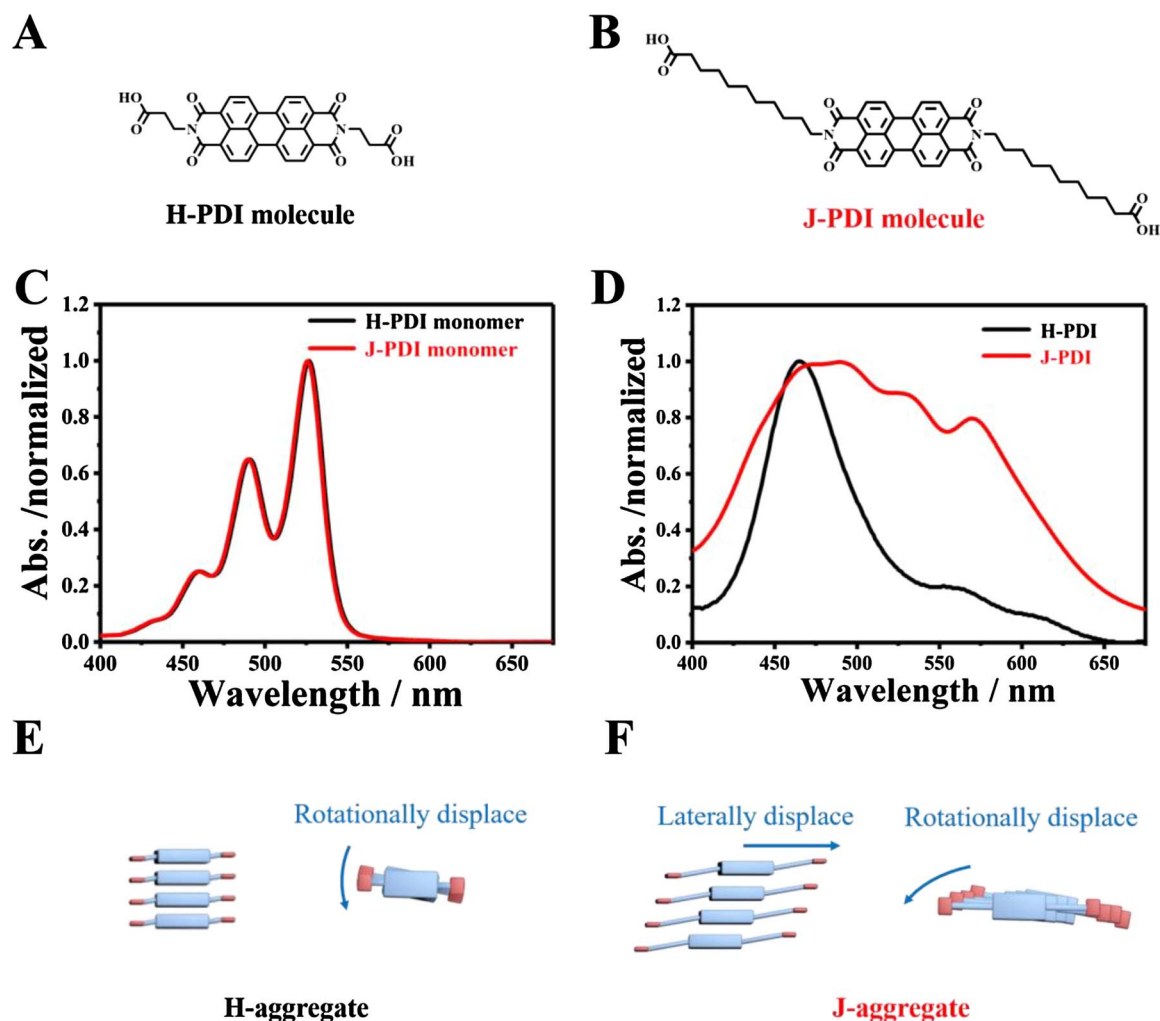
2.6. In vitro cytotoxicity assay

BALB/nu nude mice (6 weeks old) were purchased from Vital River Laboratories (Beijing, China), and all animals received care in compliance with the guidelines outlined in the Guide for the Care and Use of Laboratory Animals. The procedures were approved by the University of Science and Technology of China's Animal Care and Use Committee. The xenograft tumor model was generated by injecting MDA-MB-231 cells (2 × 106 per mouse) in the mammary fat pad of each mouse. When the tumor volumes reached about 100 mm^3, the mice received a subcutaneous injection of 10 μl (500 μg/mL) of aqueous suspension of H/J-PDI. The tumor site was irradiated under 600 nm (220 mW/cm^2) for 10 min at 12 h postinjection. Tumor growth was monitored by measuring the perpendicular diameter of the tumor using calipers. The estimated volume was calculated according to the following formula: tumor volume (mm^3) = 0.5 × length × width^2. At the last time point, the mice were sacrificed and the tumor tissue were excised and imaged.

3. Results and discussion

3.1. Supramolecular packing structure

Two PDI (perylenetetracarboxylic diimide) derivatives modified with different length of linear carboxy-substituent side-chains (Scheme S1) are employed to construct H/J-type aggregated PDI supramolecular nanostructures [34]. The PDI derivatives studied here are designated as H-PDI (Fig. 1A) and J-PDI (Fig. 1B). The structure of side-chains in H-PDI and J-PDI molecules can be confirmed by FT-IR spectra and TGA curves as shown in Fig. S1. As the two nitrogen positions at the imides of PDI are nodes in the π-orbital wave function, the introduction of side-chain impose little effect on the electronic properties of PDI molecule, offering wide options to modify the π-π stacking arrangement, which in turn allows for investigating the structure-property relationship of PDI

A

HO–O

H-PDI molecule

B

HO–O

J-PDI molecule

C

D

E

Rotationally displace

H-aggregate

F

Laterally displace   Rotationally displace

J-aggregate

Fig. 1. (A, B) Molecular structures of H-PDI (A) and J-PDI (B). (C) UV–vis spectra of H-PDI monomer and J-PDI monomer. (C) UV–vis spectra of H-PDI and J-PDI nanostructures. (E, F) Supramolecular packing model of H-aggregates (E) and J-aggregates (F). (For interpretation of the references to colour in text, the reader is referred to the web version of this article).

supramolecular nanostructures [35,36]. The H-PDI and J-PDI supramolecular nanostructures are prepared via a pH triggered hydro gelation method developed by Zang et al. [34].

UV–vis absorption and fluorescence spectra of PDIs are sensitive to their molecular packing [37] and, therefore, have been widely used to study their supramolecular π-π stacking [35,38]. The UV–vis spectra of H-PDI and J-PDI are shown in Fig. 1C and D, and the spectral parameters are summarized in Table S1. The absorption spectra of H-PDI and J-PDI monomer are almost identical, which exhibit typical spectroscopic features of monomeric PDI (Fig. 1C) [25]. After self-assembling, the maximum absorption band of H-PDI strongly blue-shifted for 62 nm (465 nm) compared with monomer, and the fine curve structure of absorption spectrum is lost (Fig. 1D, black line), indicating the formation of H-aggregates during the supramolecular self-assembly [39]. In contrast, the absorption spectrum of J-PDI presents a new absorption at about 578 nm (Fig. 1D, red line). Such significant red-shifted absorption is typical sign of J-aggregates [32,40–42]. The loss of fine curve structure in absorption spectrum of H-PDI means the transformation from discrete energy level to continuous energy level. Therefore, compared with J-PDI, H-PDI shows more semiconductor characteristics.

The fluorescence spectra (excited at 468 nm) of H-PDI and J-PDI are shown in Figs. S2 and S3. The emission maximum of H-PDI red-shifts distinctively to 735 nm relative to that of J-PDI (720 nm, Fig. S2). With monomeric PDI (Φf = 100%) standard reference, the fluorescence quantum yield of J-PDI is measured to be 4.79%. Nevertheless, in H-

PDI, the fluorescence is almost entirely quenched (Table S1). Moreover, the fluorescence lifetimes measured for J-PDI are significantly shorter than that of H-PDI (Fig. S3). Normally, the lowest-energy emission is forbidden in H-aggregates, but dipole-allowed for J-type aggregation, which results in the blue-shift of UV–vis absorption, red-shift of fluorescence emission and the fluorescent quenching in H-aggregates [17,32].

Generally, PDI molecules primarily stack in a face-to-face arrangement in H-aggregates, while J-aggregates form when molecules predominantly stack head-to-tail [17]. It is worth noting that the blue shift (62 nm) on the maximum absorption band of H-PDI is much larger than that reported previously for other H-aggregates of PDIs [35,43]. Such extra-large blue shift can be attributed to the in-plane torsion between the adjacent PDI rings [31]. Therefore, H-PDI molecules stack in face-to-face arrangement with a small in-plane torsion between two adjacent molecules (Fig. 1E) [28,31]. In contrast, J-PDI molecules stack in head-to-tail model with both laterally and rotationally defect occurring between two adjacent molecules (Fig. 1F) [28,31]. Laterally displaced in J-PDI greatly reduce the density of electron cloud overlap [29]. Compared with J-PDI, H-PDI has higher π-conjugation because of its higher density of electron cloud overlap. Higher π-conjugation means faster carrier mobility and higher carrier separation efficiency, which has a great influence in photocatalytic mechanism and activity of PDI.

The morphology of H-/J-PDI nanostructures are investigated by Transmission electron micrograph (TEM). It is clear that the H-PDI molecules assembles into nanofibers with hundreds of nanometers to
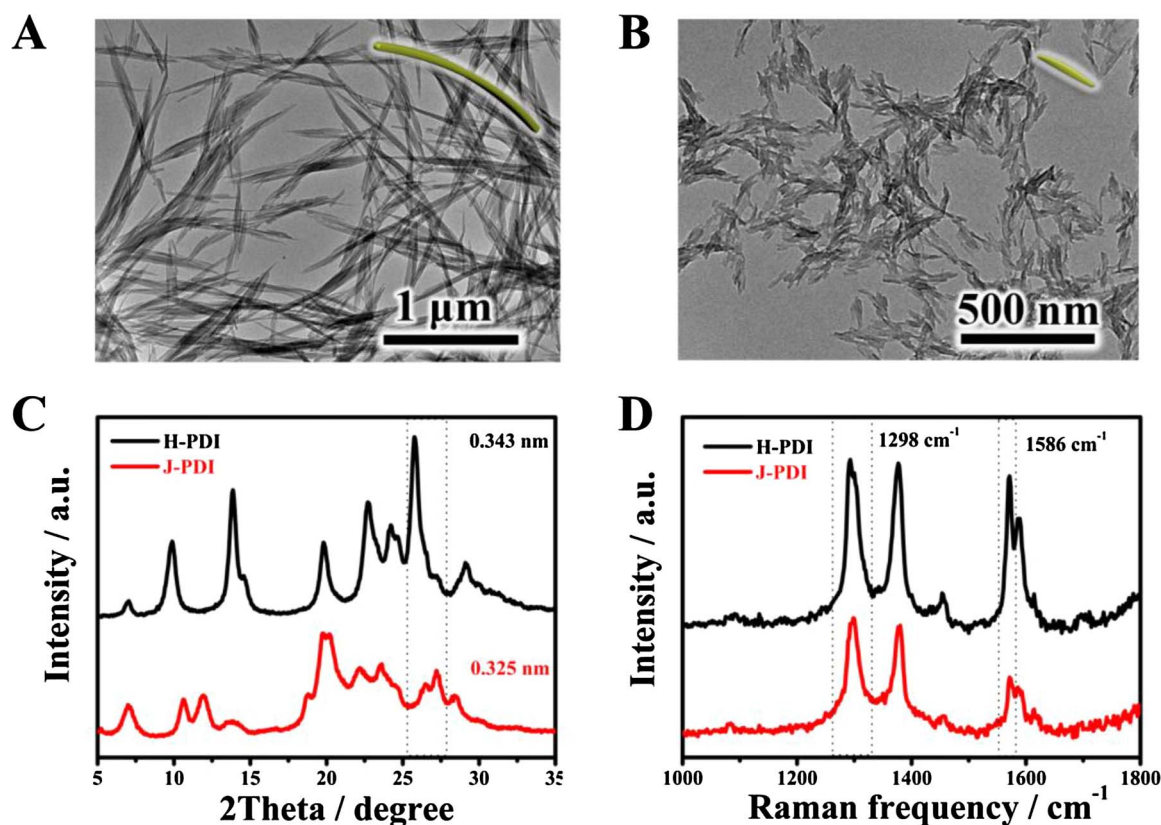
Fig. 2. (A, B) TEM images of H-PDI (A) and J-PDI (B) supramolecular nanomaterials. (C, D) XRD patterns spectra (C) and Raman spectra (D) of H-PDI and J-PDI.

micrometers in length (Fig. 2A). The diameter ratio of H-PDI nanofibers is more than 25. In contrast, J-PDI tends to form nanorods with lower diameter ratio less than H-PDI (Fig. 2B). The BET surface area of H-PDI and J-PDI are 10.05 m^2/g and 16.02 m^2/g (Table S2), respectively. J-PDI has a larger specific surface area due to its smaller nanoscale. According to the results of HRTEM (Fig. S4), both H-PDI and J-PDI have no long-range order structures. As reported in the literature, PDIs with different substituents at imide positions could pack in different patterns in crystals due to the different interactions between the adjacent molecules [26]. Due to difference of side-chain hydrophobicity-hydrophilicity and steric hindrance, the crystal nucleation and growth speed of H-PDI and J-PDI molecules are quite different in water. For the H-PDI molecule with short side-chains, well-defined nanofibers can simply be obtained with favorable molecular packing owing to the slow nucleation rate and long crystal growth time (Fig. 2A). However, for the J-PDI molecule with long side-chains, the aggregation often proceeds too fast for the molecular assembly to grow along one direction due to the strong hydrophobic interaction and enhanced intermolecular association, thus leading to the formation of chunky aggregates rather than nanowires/nanofibers (Fig. 2B) [35]. For quasi one-dimensional stacking structure, the degree of π-π stacking is proportional to the diameter ratio of 1D nanostructures. The larger diameter ratio means higher π-conjugated [28].

The difference in π-conjugated of H-PDI and J-PDI can also be confirmed by XRD and Raman analysis (Fig. 2C and D). As shown in Fig. 2C, XRD peaks between 24° and 28° are corresponded to typical π-π stacking distance between the PDI perylene skeletons with d-spacing of 0.32–0.37 nm [34]. It is clear that the relative peak intensity of H-PDI is much higher than that of J-PDI, indicating that the H-PDI has higher degree of π-π stacking than that of J-PDI. As shown in Fig. 2D, the Raman active normal mode at larger wavenumber (1586 cm^{-1}) corresponds to the shrinking of the stretching of the in-plane C=C/C−C and the perylene aromatic ring core coupled to the C=O antisymmetric, which is sensitive to the π-π stacking [44]. In contrast, Raman mode of

C−H in plane bending at 1298 cm^{-1} is insensitive to the π-π stacking intermolecular interactions [44]. It is clear that the relative intensity of 1586 cm^{-1} to 1298 cm^{-1} in H-PDI sample was higher than that of J-PDI, indicating that the H-PDI has higher π-conjugated. Higher π-π stacking results in long-range π electrons delocalization, which is benefit to the migration and separation of charge carriers.

3.2. Photoenergy conversion mechanism

The ESR (electron paramagnetic resonance) technique is employed to detect the ROS generation by H-PDI and J-PDI under irradiation. TEMP (2,2,6,6-tetramethyl-1-piperidine) and DMPO (5,5-dimethyl-1-pyrroline N-oxide) are used as $^1O_2$ and $\cdot O_2^-$ (or $\cdot OH$) trappers [45]. As illustrated in Fig. 3 and S5, characteristic $\cdot O_2^-$-induced and $^1O_2$-induced signal are observed both in H-PDI and J-PDI under irradiation while no $\cdot OH$-induced signal can be found. However, the enhancement of $\cdot O_2^-$ signal intensity for J-PDI is almost negligible after irradiation (Fig. 3B), and the signal intensity of H-PDI is about 4.7 times higher than that of J-PDI (Figs. 3A and S5A). In contrast, J-PDI shows a robust ability to produce singlet oxygen. The intensity increases obviously for J-PDI after irradiation (Fig. S5B), while almost no change can be found in signal intensity for H-PDI before and after irradiation (Fig. 3C). The $^1O_2$-induced signal intensity of J-PDI is about 5.1 times higher than that of H-PDI (Fig. 3D).

The distinction of $^1O_2$ generation for H-PDI and J-PDI can be further confirmed through a chemical trapping experiment with 1,3-diphenylisobenzofuran (DPBF) as the trapping agent and Rose Bengal (RB) as the standard photosensitizer ($^1O_2$ quantum yield $\Phi_{RB} = 0.86$ in ethanol) [46]. The absorption of DPBF at 410 nm was recorded under irradiation (600 ± 15 nm) to obtain the decay rate of the photosensitizing process (Fig. 4). As shown in Fig. 4A, the absorbance of the DPBF solution at 410 nm decreases gradually with prolonged irradiation time in the presence of J-PDI under irradiation, indicating that the J-PDI can generate $^1O_2$ (Fig. 4B). In contrast, H-PDI has no activity for
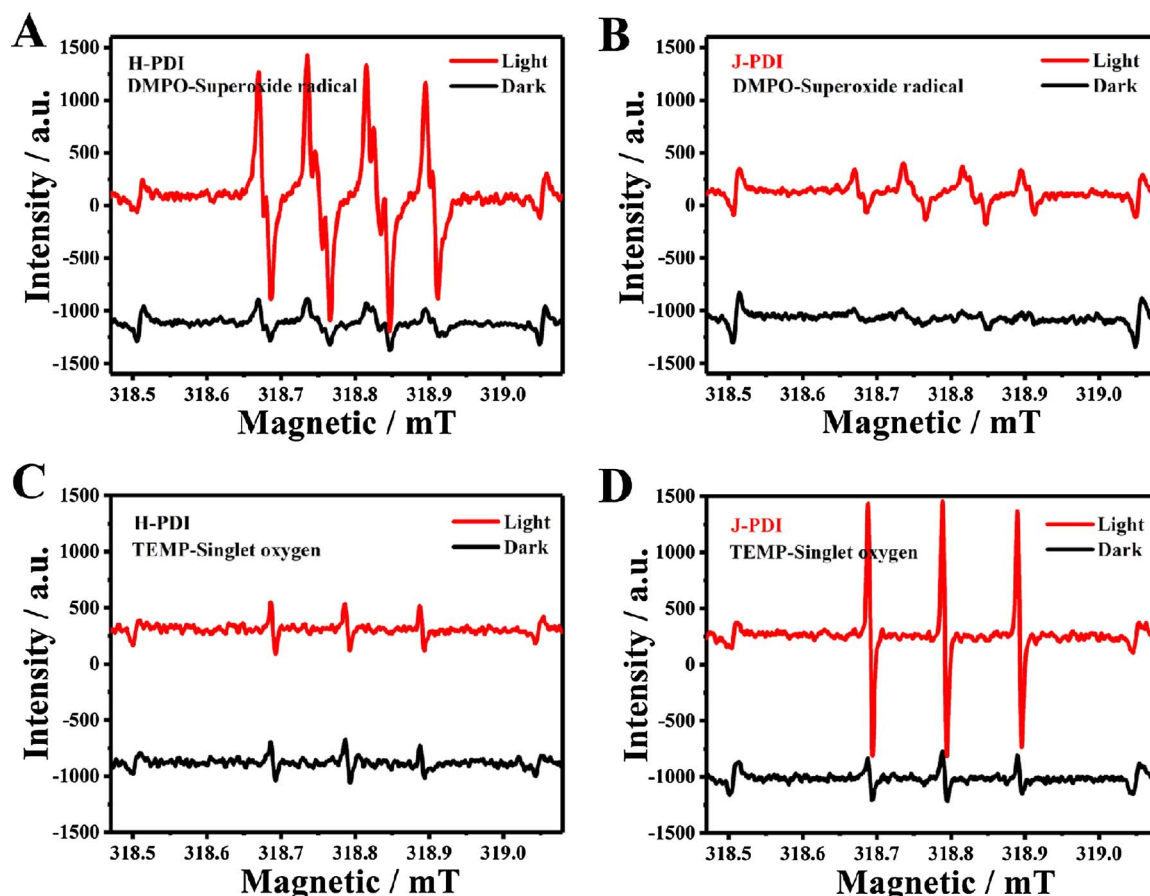
Fig. 3. (A, B) The ESR signals of (A) superoxide radical ($\cdot O_2^-$) and (B) singlet oxygen ($^1O_2$) in H-PDI and J-PDI obtained with (solid line) and without (dotted line) irradiation, respectively.

the photosensitization of DPBF (Fig. 4C). The $^1O_2$ quantum yield of the PDI (Φ_{PDI}) was calculated using the following formula:

$$\Phi_{H/J-PDI} = \Phi_{RB} * K_{H/J-PDI} * A_{RB}/(K_{RB} * A_{H/J-PDI})$$

where K_{PDI} and K_{RB} are the decomposition rate constants of DPBF by the H/J-PDI and RB, respectively. $A_{H/J-PDI}$ and A_{RB} represent the light absorbed by H/J-PDI and RB, respectively, which are determined by integration of the optical absorption bands in the wavelength range 400–700 nm. The $^1O_2$ quantum yields of the J-PDI are calculated to be 0.66 at 600 ± 15nm (Fig. 4D).

To further investigate the active species of H-PDI and J-PDI, chemical trapping experiments are carried out during the photocatalytic degradation of BPA with the addition of $^1O_2$ scavenger (sodium azide, NaN_3) [47], $\cdot O_2^-$ scavenger (p-benzoquinone, p-BQ) [48,49], h^+ scavenger (potassium iodide, KI) [48,50] and $\cdot OH$ scavenger (tert-Butanol, t-BuOH) [48,50,51], respectively (Fig. 5). The addition of t-BuOH has no effect on the degradation of phenol for H-PDI and J-PDI, indicating that both H-PDI and J-PDI cannot generate the $\cdot OH$, which confirms the results of ESR. In contrast, the degradation rate decreases drastically for both H-PDI and J-PDI with injecting nitrogen into the reaction system (low oxygen concentration). The result reveals the existence of oxygen dependent active species of H-PDI and J-PDI. In H-PDI, the addition of NaN_3 also has no effect on the degradation of phenol while the degradation rate reduces drastically with the addition of KI and p-BQ (Fig. 5A and C), indicating that the h^+ and $\cdot O_2^-$ are the main oxidative species for H-PDI. On the contrary, the degradation rate decreases drastically for J-PDI after trapping $^1O_2$. This result reveals that the main active specie of J-PDI is $^1O_2$ (Fig. 5B and D).

As an excited state of molecular oxygen, the $^1O_2$ is commonly generated via EnT from a triplet excited state (T1) photosensitizer to

$^3O_2$ under illumination [52–54]. Whereas, the $\cdot O_2^-$ is normally generated via ET of photoinduced electron from conduction band to molecular oxygen under irradiation, accompanied by the generation of holes at the valance band of semiconductor [52–54]. Therefore, the main distinction between EnT and ET is whether the photoinduced carriers' separation emerges under illumination. The photocurrent test and surface photovoltage spectroscopy (SPV) are effective techniques to study the carrier separation efficiency of photocatalyst [55,56]. Here, the photocurrent tests are carried out without bias under visible light (> 420 nm). As shown in Fig. 6A, H-PDI exhibits much higher current intensity, which is 7.7 times higher than that of J-PDI. Similarly, the photovoltaic response intensities of H-PDI are significantly higher than that of J-PDI (Fig. 6B). Furthermore, the OER curves of H-PDI and J-PDI also reveal that the internal resistance of H-PDI is lower than that of J-PDI, in which H-PDI shows smaller initial voltage and higher curve slope in OER curve (Fig. S6). The higher photocurrent, photovoltaic response intensities and lower internal resistance reveal that the H-PDI has a higher carrier separation efficiency than that of J-PDI, which is attributed to the higher π electrons delocalization of H-aggregates.

The supramolecular electronic structures of H-PDI and J-PDI are investigated combined with UV–vis absorption spectra, UV–vis diffuse reflection spectra (DRS), X-ray photoemission spectroscopy (XPS) valence band spectra and Mott-Schottky plots measurements (Fig. 7). The energy band and energy level parameters of H-PDI and J-PDI are summarized in Table S3. Different from the PDI molecule with discrete absorption peak, the UV–vis diffuse reflection spectra of H-PDI and J-PDI are similar to an intrinsic absorption of inorganic semiconductor (Fig. 7A), indicating that both H-PDI and J-PDI have band-like electronic structures with certain bandwidths for valence and conduction bands. The absorption edge spectrum of H-PDI is about 734 nm, which
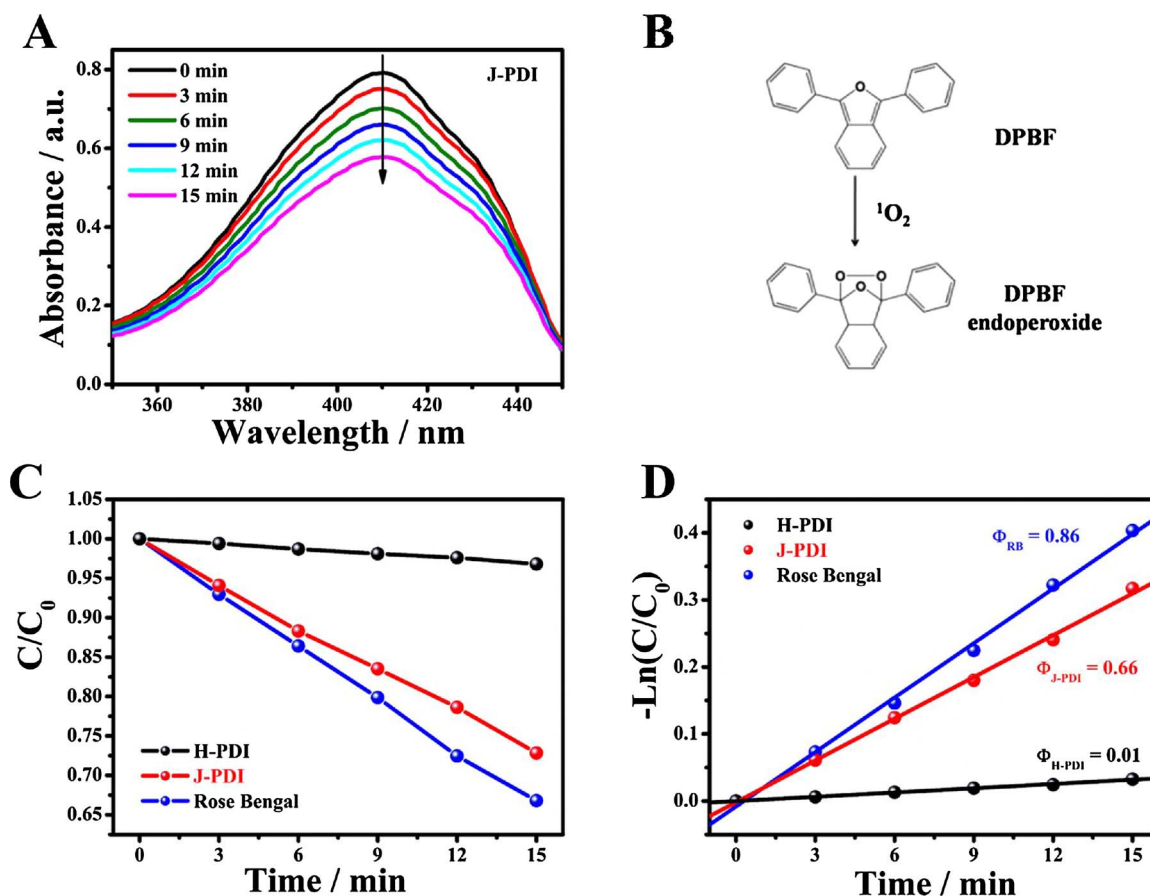
Fig. 4. (A) Time-dependent absorption spectra of the DPBF with J-PDI (A) under irradiation. (B) Illustration of the reaction from DPBF to DPBF endoperoxide by singlet oxygen. (C) The degradation plot of DPBF at 410 nm in the presence of H-PDI, J-PDI and Rosel Bengal (RB) under irradiation (600 ± 15 nm). (D) The first order kinetics curve fitting of DPBF at 410 nm in the presence of H-PDI, J-PDI and Rosel Bengal (RB) under irradiation (600 ± 15 nm).

red-shifts for 39 nm compared with J-PDI (695 nm). The bandgaps of H-PDI and J-PDI are estimated to be 1.69 and 1.78 eV, respectively. It is clear that H-PDI (1.69 eV) has a narrower bandgap than that of J-PDI (1.78 eV). As is known to all, orbital splitting usually occurs with overlap of electron cloud. Therefore, higher π electron conjugated normally means a narrower band gap [7]. Our previous work has also proved that higher π electron conjugated of PDI leads to a narrower bandgap [20]. Thus, it is reasonable to ascribe the narrower bandgap of H-PDI relative to the J-PDI to the larger π-conjugated system of H-aggregates.

The bottom of conduction band (CB) for H-PDI and J-PDI can be estimated by the Mott-Schottky plots. As shown in Fig. 7B, the flat band potential (E_{fb}) for H-PDI and J-PDI nanofibers are −0.21 V, −0.42 V vs. SCE (pH = 7), respectively. For n-type semiconductors, the CB is 0.2 V higher than that of Fermi level. Therefore, the CBM of H-PDI and J-PDI at normal hydrogen electrode (NHE, pH = 7) can be calculated using the following equation:

$$E_{CB}(\text{NHE, pH} = 7) = E_{fb}(\text{SCE, pH} = 7) + 0.24 - 0.2$$

The results reveal that the CB position of H-PDI and J-PDI are about −0.17 V and −0.38 V vs. NHE. According to the band gap (1.74 eV and 1.69 eV), the valence band (VB) position of H-PDI and J-PDI are estimated to be +1.52 and +1.40 V vs. NHE. The schematic diagram of energy level of H-PDI and J-PDI are summarized in Fig. 7D. The CB/VB of H-PDI and J-PDI are evaluated to be −0.17/+1.52 V and −0.38/+1.40 V. It is clear that the VB position of H-PDI is deeper than that of J-PDI. This result can be further confirmed by X-ray photoemission spectroscopy (XPS) valence band spectra. As shown in Fig. 7C, the VB positions of H-PDI and J-PDI are about +2.20 and +2.03 eV. The

deeper VB position means stronger oxidation ability of holes for photooxidation. Noted that the VB positions of H-PDI or J-PDI are shallower than the potential of hydroxyl radical ($E°(H_2O/·OH) = +2.27$ eV) [57], which is the possible reason to the unavailable of hydroxyl radical for H-PDI and J-PDI. According to CB positions, singlet oxygen (E0 ($·O_2^-/{}^1O_2$) = +0.34 eV) are thermodynamic available both to H-PDI and J-PDI. However, no singlet oxygen can be found in H-PDI. These results reveal that the thermodynamic is not the main factor to the ET or EnT in PDI supramolecular nanomaterials. The lack of EnT process in H-aggregates may be attributed to the highly carrier separation efficiency and forbidden low-energy excitonic transition, which needs further investigation.

3.3. Photooxidation and anticancer performance

Different mechanism of ET/EnT determines the application prospects of H-aggregated and J-aggregated PDI. The photocatalytic oxidation performance of H-PDI and J-PDI are evaluated by photocatalytic degradation of organic pollutants (phenol, methylene blue/MB and methyl orange/MO) and oxygen evolution under visible light (> 420 nm). As shown in Fig. 8A, H-PDI shows excellent performance of phenol degradation, which could degrade more than 50% of phenol in 4 h. Whereas, the degradation of phenol by J-PDI is negligible. The apparent reaction rate of H-PDI is calculated to be $0.19534 h^{-1}$, which is about 13.5 times higher than that of J-PDI. Similarly, H-PDI shows more superior photocatalytic activities for the degradation of MB (cationic dye) and MO (anionic dye) (Figs. 8B and S7). It is worth noting that both H-PDI and J-PDI are found to possess greater removal ability for cationic dye (MB) than anionic dye (MO), which can be attributed to
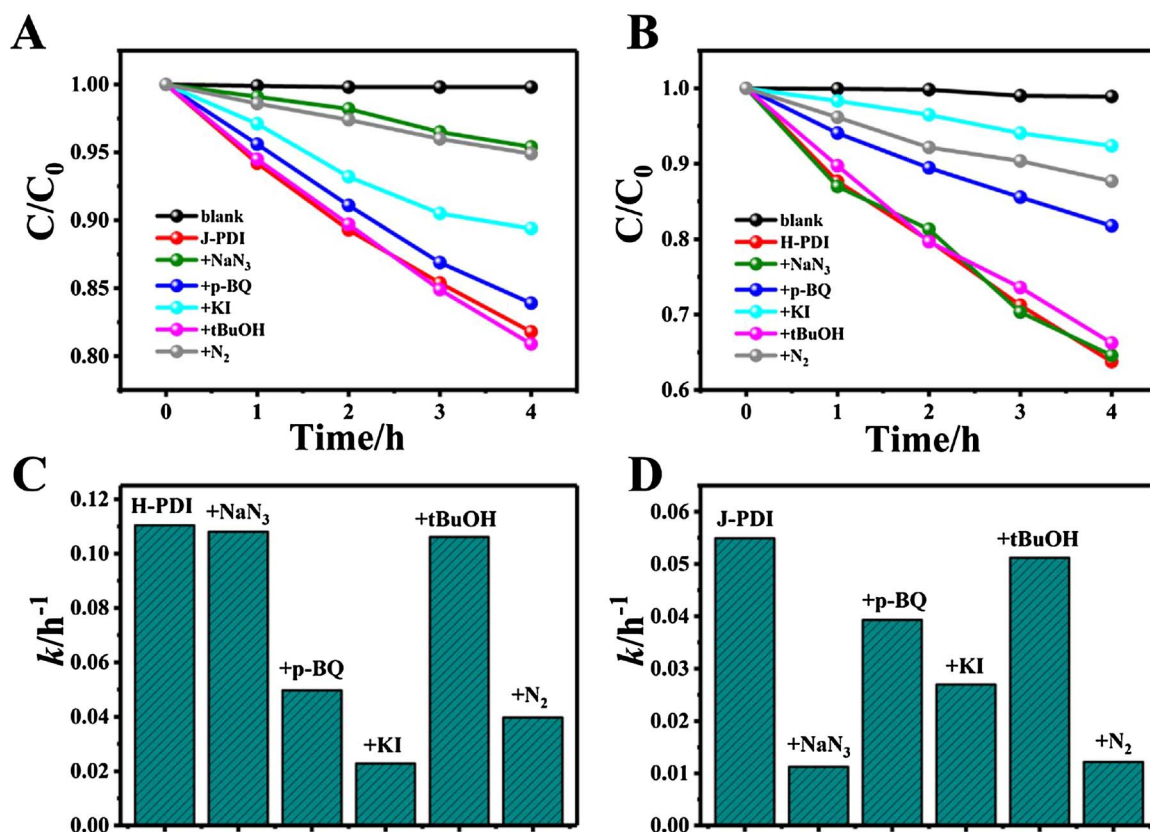
Fig. 5. (A, B) Plots of photogenerated carriers trapping in the system of photodegradation of BPA by H-PDI (A) and J-PDI (B). (C, D) The degradation rate constants *k* of BPA by H-PDI (C) and J-PDI (D) in the carriers trapping experiments.

their strong adsorption ability of cationic dye (Fig. S8) owing to the negative surface electric property revealed by zeta potential measurement (Table S4). The oxygen evolution tests of H-PDI and J-PDI are carried out under visible light irradiation with assistance of IrO_2. Similarly, H-PDI exhibits more superior photocatalytic activities, which is about 7.6 times higher than that of J-PDI (Fig. S9).

The in vitro anticancer activities of H-PDI and J-PDI are studied using a standard 3-(4,5-dimethylthiazol-2-yl)-2,5-diphenyl-2H-tetrazolium hydrobromide (MTT) assay. In these experiments, HeLa cells are irradiated under 475 or 600 ± 15 nm (power density, 220 mW/cm^2) for a constant duration of 10min with catalysts from 62.5 to 750 μg/mL. Compared with the classic photosensitizer Protoporphyrin IX (PpIX), both H-PDI and J-PDI show higher biocompatibility and lower cytotoxicity in the dark, which has little effect on the survival of HeLa cells

even at a concentration of 750 μg/mL (Fig. S10). Furthermore, J-PDI shows higher photostability compared with PpIX under irradiation (Fig. S11). As shown in Fig. 9A and S12, J-PDI shows higher cell growth inhibition than that of H-PDI under 475 or 600 ± 15 nm. The optimal anticancer activity of J-PDI can be observed at a concentration of 500 μg/mL. The distribution of J-PDI in Hela cell is investigated through nucleus fluorescence images stained by Hoechst 33,342. As shown in Fig. S13, cell fluorescence image demonstrates that the J-PDI labels only the cytoplasm and not the nucleus. The above results verify that J-PDI exhibits potential application in photocatalytic anti-cancer treatment due to its high Hela cells growth inhibition efficiency, low cytotoxicity and high photostability.

The production of intracellular ROS inside the cancer cells can be further detected by using a cell permeable fluorescent dye
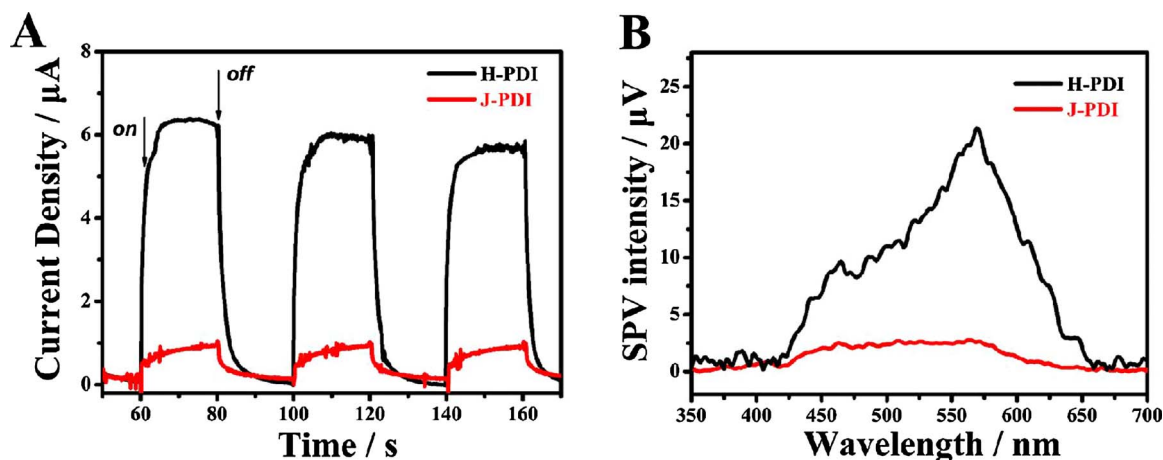

Fig. 6. (A, B) Photocurrent responses curves (A) and surface photovoltage spectroscopy (B) of H-PDI and J-PDI.
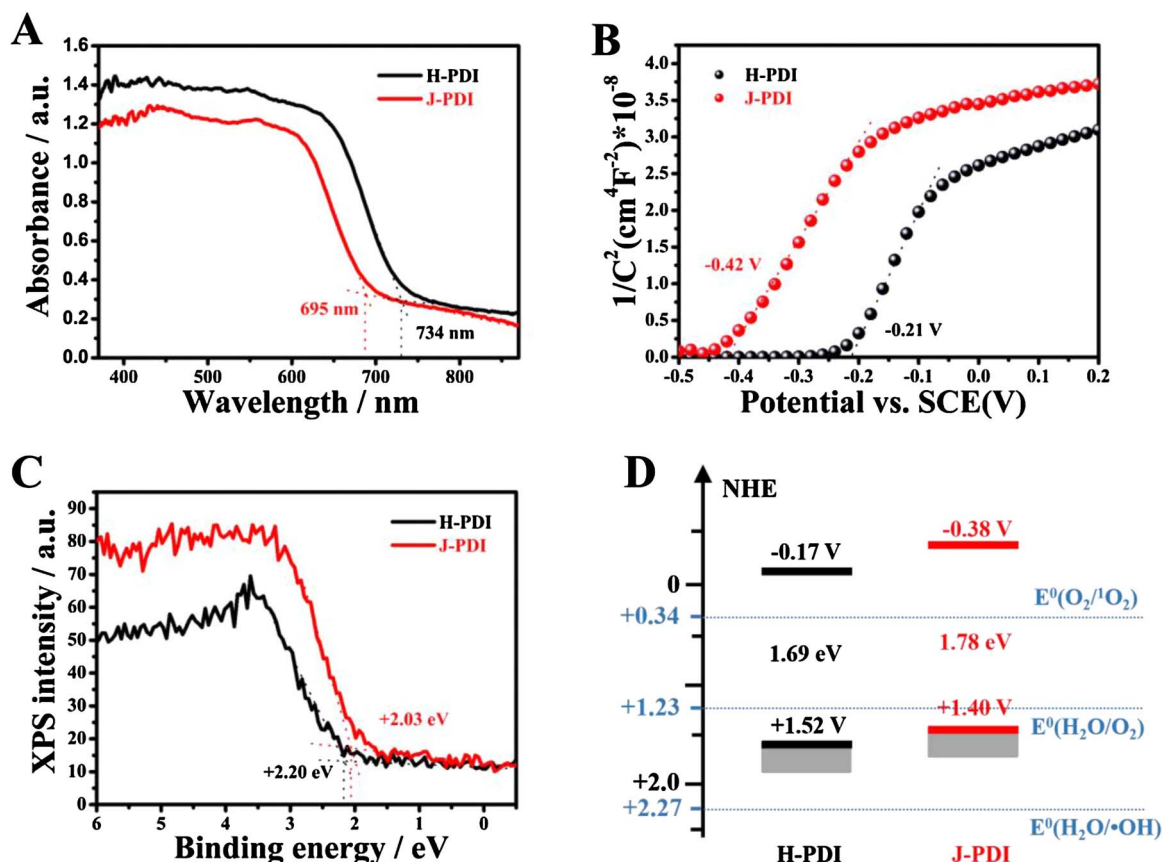
Fig. 7. (A, B, C) UV–vis diffuse reflection spectra (A), Mott – Schottky plots (B) and X-ray photoemission spectroscopy (XPS) valence band spectra (C) of H-PDI and J-PDI; counter electrode: Pt. electrolyte: 0.1 M Na_2SO_4, frequency: 100 kHz. (D) Diagram representing experimentally evaluated VB and CB levels of H-PDI and J-PDI.

dichlorofluorescein (DCF). As shown in Fig. S14, only weak red fluorescence can be found without light irradiation, while strong green fluorescence was observed after irradiation, indicating the generation of ROS inside the cells during irradiation with light. The intracellular singlet oxygen production by J-PDI under light irradiation would induce cells apoptosis. To further investigate the main active species in the in vitro anticancer tests, chemical trapping experiments are carried out. Similarly, NaN_3, p-BQ and KI are used as $^1O_2$, O_2^- and h^+ scavenger, respectively. These masking agents have no effect on the survival of HeLa cells under light irradiation without J-PDI. As shown in Fig. 9B, the addition of p-BQ and KI also have little effect on anti-cancer activities, while the anti-cancer activity reduces drastically with the

addition of NaN_3, indicating that the $^1O_2$ is the main active specie for photocatalytic anti-cancer treatment in J-PDI.

The performance of the H-PDI and J-PDI for in vivo photocatalytic anticancer treatment is evaluated using female BALB/nu mice with subcutaneous breast cancer xenografts as an animal model. After the average tumor volume exceeded $100 \, mm^3$, 15 mice are randomly divided into three groups, and each mouse is injected with $10.0 \, \mu L$ of the suspension of H-PDI, J-PDI $(500 \, \mu g/mL)$ or saline. These mice are exposed to the $600 \pm 15 \, nm$ light for 10 min at the power density of $220 \, mW/cm^2$. The tumor growth was significantly hindered after being injected with H-PDI or J-PDI (Fig. 9C). Compared with H-PDI, J-PDI shows a stronger inhibition for tumor. The tumors were festered after
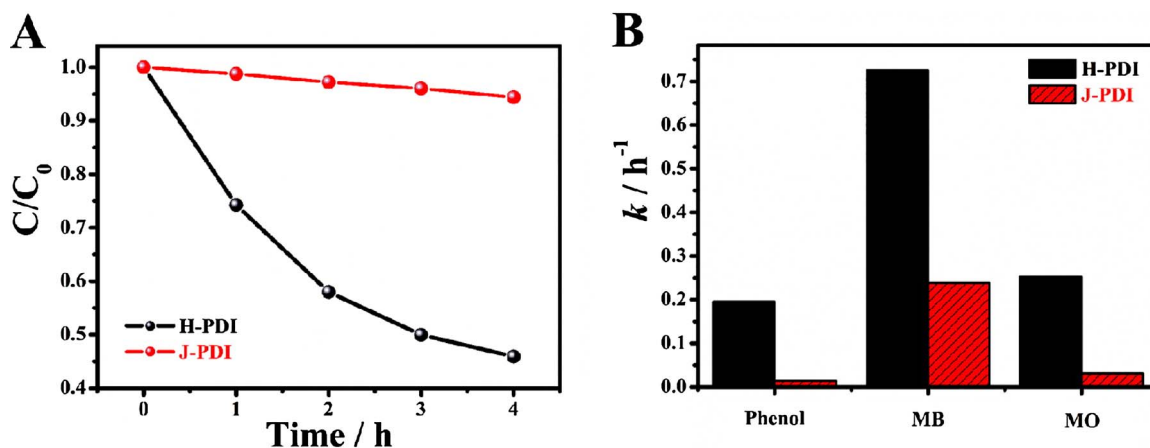

Fig. 8. (A) Photodegradation curves for phenol (5 ppm) over H-PDI and J-PDI under visible light. (B) The degradation rate constants k of phenol, methylene blue (MB) and methyl orange (MO) by H-PDI and J-PDI.
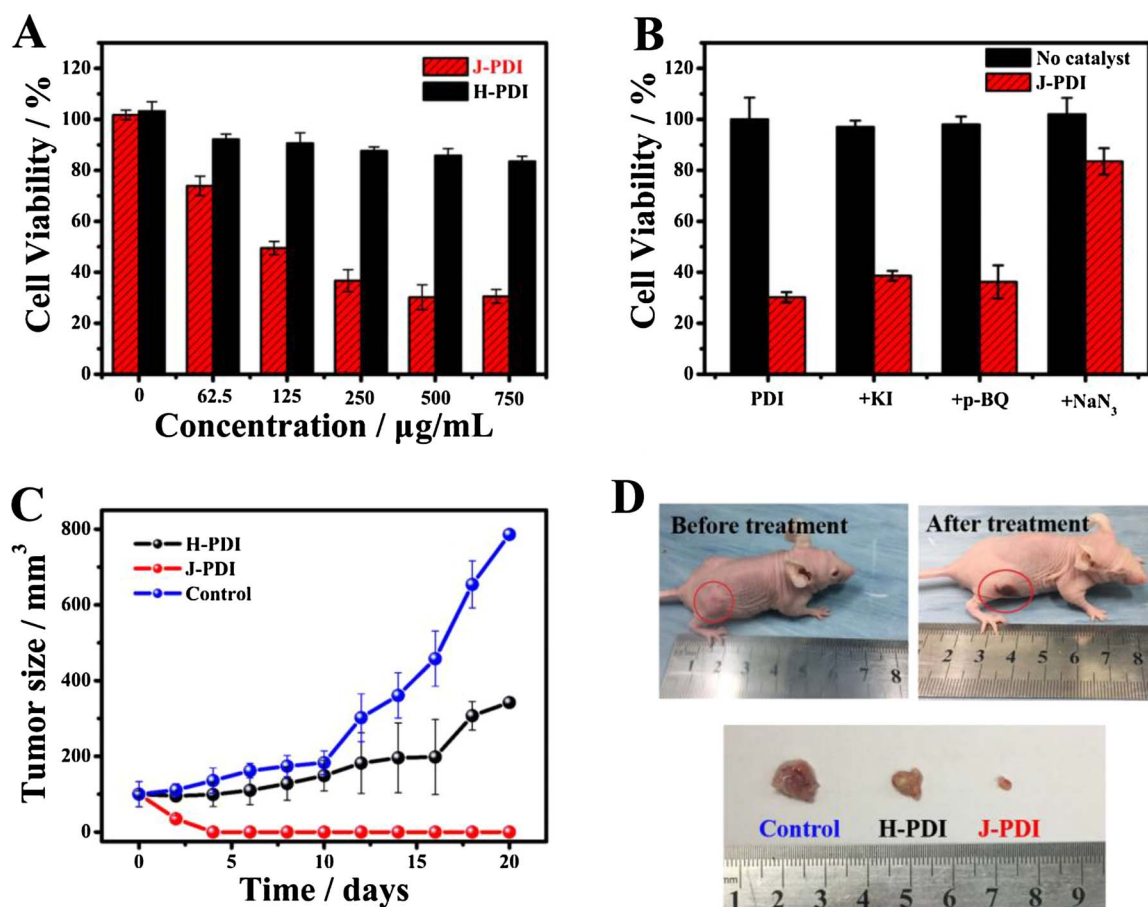
Fig. 9. (A) In vitro viability of HeLa cells with different concentrations of H-PDI and J-PDI at 600 ± 15 nm. (B) Chemical trapping experiments for $^1O_2$, $\cdot O_2^-$ and h^+ in the in vitro anticancer tests. (C) Time-dependent tumor growth in a murine tumor model after treated with H-PDI and J-PDI. (D) Photographs of mice and tumors after treated with H-PDI and J-PDI.

treatment with J-PDI. As expected, the volume of the tumor is minimum after treatment with J-PDI under irradiation (Fig. 9D). Moreover, the in vivo toxicity of the H/J-PDI was also roughly estimated by monitoring the weight change of the mice in the study period, and no obvious side effects are revealed (Fig. S15). The haematoxylin and eosin (H&E) sections also demonstrate serious necrosis in the tumor tissue of the J-PDI treated group (Fig. S16).

4. Conclusion

In conclusion, the effects of H/J-type supramolecular packing on the

photoenergy transfer mechanism and photocatalytic activity of PDI supramolecular organic nanomaterials have been studied (Fig. 10). The reaction pathway of H-aggregates is proved to be ET, while EnT is found to be main reaction pathway in J-aggregates. Compared with J-aggregates, the H-aggregates has lager π-delocalization due to its less stacking defect, which leads to the narrower bandgap, deeper VB and higher mobility and separation efficiency of photo-induced carriers. As a result, excited state H-aggregates PDI mainly forms O_2^- and h^+ by ET. Whereas, excited state J-aggregates PDI mainly generates $^1O_2$ via EnT. Benefit from the stronger oxidizability of $\cdot O_2^-$ and h^+, the H-aggregates PDI shows higher water photooxidation under visible light.
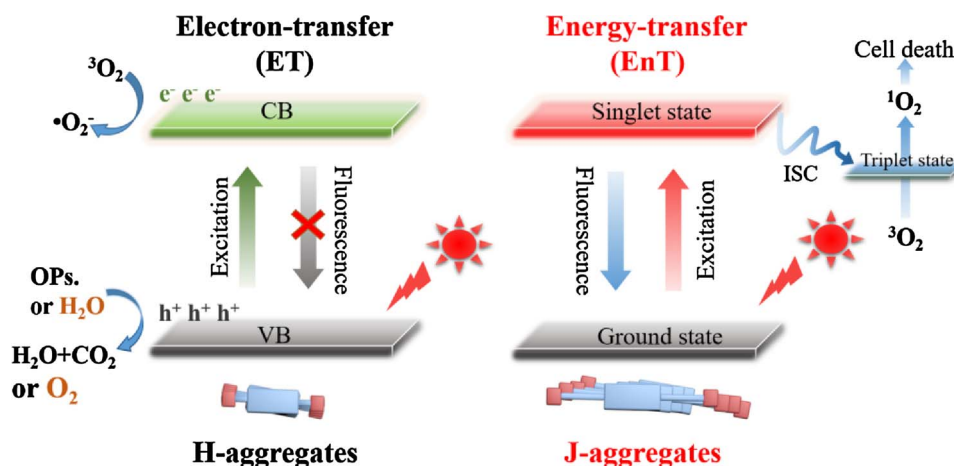

Fig. 10. Diagram representing the effect of supramolecular packing on electron-transfer (ET) and energy-transfer (EnT) in H/J-aggregated PDI photocatalysts.

Whereas, J-aggregates PDI exhibits potential application in photocatalytic anti-cancer treatment owing to its high $^1O_2$ quantum yields under red light irradiation. Our work may provide guidance for the research of supramolecular organic photocatalytic materials.

Acknowledgements

Appendix A. Supplementary data

Supplementary material related to this article can be found, in the online version, at doi:https://doi.org/10.1016/j.apcatb.2018.03.026.

References

[1] T. Zhang, W. Lin, Metal–organic frameworks for artificial photosynthesis and photocatalysis, Chem. Soc. Rev. 43 (2014) 5982–5993.

[2] S. Chen, P. Slattum, C. Wang, L. Zang, Self-assembly of perylene imide molecules into 1d nanostructures: methods, morphologies, and applications, Chem. Rev. 115 (2015) 11967–11998.

[3] C. Zhang, P. Chen, H. Dong, Y. Zhen, M. Liu, W. Hu, Porphyrin supramolecular 1D structures via surfactant-assisted self-assembly, Adv. Mater. 27 (2015) 5379–5387.

[4] L. Zang, Y. Che, J.S. Moore, One-dimensional self-assembly of planar π-conjugated molecules: adaptable building blocks for organic nanodevices, Acc. Chem. Res. 41 (2008) 1596–1608.

[5] Y. Guo, L. Xu, H. Liu, Y. Li, C.M. Che, Y. Li, Self-assembly of functional molecules into 1D crystalline nanostructures, Adv. Mater. 27 (2015) 985–1013.

[6] R.S. Sprick, J.-X. Jiang, B. Bonillo, S. Ren, T. Ratvijitvech, P. Guiglion, M.A. Zwijnenburg, D.J. Adams, A.I. Cooper, Tunable organic photocatalysts for visible-light-driven hydrogen evolution, J. Am. Chem. Soc. 137 (2015) 3265–3270.

[7] S. Ghosh, N.A. Kouamé, L. Ramos, S. Remita, A. Dazzi, A. Deniset-Besseau, P. Beaunier, F. Goubard, P.-H. Aubert, H. Remita, Conducting polymer nanostructures for photocatalysis under visible light, Nat. Mater. 14 (2015) 505–511.

[8] D. Chen, K. Wang, D. Xiang, R. Zong, W. Yao, Y. Zhu, Significantly enhancement of photocatalytic performances via core–shell structure of ZnO@ mpg-C3N4, Appl. Catal. B: Environ. 147 (2014) 554–561.

[9] Q. Hao, X. Niu, C. Nie, S. Hao, W. Zou, J. Ge, D. Chen, W. Yao, A highly efficient gC 3 N 4/SiO 2 heterojunction: the role of SiO 2 in the enhancement of visible light photocatalytic activity, Phys. Chem. Chem. Phys. 18 (2016) 31410–31418.

[10] S. Wang, L. Shang, L. Li, Y. Yu, C. Chi, K. Wang, J. Zhang, R. Shi, H. Shen, G.I. Waterhouse, Metal–organic-framework-derived mesoporous carbon nanospheres containing porphyrin-like metal centers for conformal phototherapy, Adv. Mater. 28 (2016) 8379–8387.

[11] H. Yu, R. Shi, Y. Zhao, T. Bian, Y. Zhao, C. Zhou, G.I. Waterhouse, L.Z. Wu, C.H. Tung, T. Zhang, Alkali-assisted synthesis of nitrogen deficient graphitic carbon nitride with tunable band structures for efficient visible-light-driven hydrogen evolution, Adv. Mater. (2017) 29.

[12] J. Chen, D. Zhao, Z. Diao, M. Wang, S. Shen, Ferrites boosting photocatalytic hydrogen evolution over graphitic carbon nitride: a case study of (Co, Ni)Fe2O4 modification, Sci. Bull. 61 (2016) 292–301.

[13] P. Guo, P. Chen, W. Ma, M. Liu, Morphology-dependent supramolecular photocatalytic performance of porphyrin nanoassemblies: from molecule to artificial supramolecular nanoantenna, J. Mater. Chem. 22 (2012) 20243–20249.

[14] C. Fu, P.J. Beldon, D.F. Perepichka, H-bonding control of supramolecular ordering of diketopyrrolopyrroles, Chem. Mater. 29 (2017) 2979–2987.

[15] G.S. Thool, K. Narayanaswamy, A. Venkateswararao, S. Naqvi, V. Gupta, S. Chand, V. Vivekananthan, R.R. Koner, V. Krishnan, S.P. Singh, Highly directional 1D supramolecular assembly of new diketopyrrolopyrrole-based gel for organic solar cell applications, Langmuir 32 (2016) 4346–4351.

[16] A.S. Weingarten, R.V. Kazantsev, L.C. Palmer, M. McClendon, A.R. Koltonow, A.P. Samuel, D.J. Kiebala, M.R. Wasielewski, S.I. Stupp, Self-assembling hydrogel scaffolds for photocatalytic hydrogen production, Nat. Chem. 6 (2014) 964–970.

[17] M. Más-Montoya, R.A. Janssen, The effect of H-and J-aggregation on the photophysical and photovoltaic properties of small thiophene–pyridine–dpp molecules for bulk-heterojunction solar cells, Adv. Funct. Mater. 27 (2017).

[18] A.S. Weingarten, R.V. Kazantsev, L.C. Palmer, D.J. Fairfield, A.R. Koltonow, S.I. Stupp, Supramolecular packing controls H2 photocatalysis in chromophore amphiphile hydrogels, J. Am. Chem. Soc. 137 (2015) 15241–15246.

[19] D. Liu, J. Wang, X. Bai, R. Zong, Y. Zhu, Self-assembled PDINH supramolecular system for photocatalysis under visible light, Adv. Mater. 28 (2016) 7284–7290.

[20] J. Wang, W. Shi, D. Liu, Z. Zhang, Y. Zhu, D. Wang, Supramolecular organic nanofibers with highly efficient and stable visible light photooxidation performance, Appl. Catal. B: Environ. 202 (2017) 289–297.

[21] W. Wei, D. Liu, Z. Wei, Y. Zhu, Short-range π–π stacking assembly on P25 TiO2 nanoparticles for enhanced visible-light photocatalysis, ACS Catal. 7 (2017) 652–663.

[22] S. Chen, D.L. Jacobs, J. Xu, Y. Li, C. Wang, L. Zang, 1D nanofiber composites of

[23] perylene diimides for visible-light-driven hydrogen evolution from water, RSC Adv. 4 (2014) 48486–48491.

[23] S. Chen, C. Wang, B.R. Bunes, Y. Li, C. Wang, L. Zang, Enhancement of visible-light-driven photocatalytic H 2 evolution from water over gC 3 n 4 through combination with perylene diimide aggregates, Appl. Catal. A: Gen. 498 (2015) 63–68.

[24] V. Kunz, V. Stepanenko, F. Würthner, Embedding of a ruthenium (II) water oxidation catalyst into nanofibers via self-assembly, Chem. Commun. 51 (2015) 290–293.

[25] F. Würthner, Perylene bisimide dyes as versatile building blocks for functional supramolecular architectures, Chem. Commun. (2004) 1564–1579.

[26] C. Li, H. Wonneberger, Perylene imides for organic photovoltaics: yesterday, today, and tomorrow, Adv. Mater. 24 (2012) 613–636.

[27] Z. Zhang, R. Ma, L. Shi, Cooperative macromolecular self-assembly toward polymeric assemblies with multiple and bioactive functions, Accounts. Chem. Res. 47 (2014) 1426–1437.

[28] P.M. Kazmaier, R. Hoffmann, A theoretical study of crystallochromy. Quantum interference effects in the spectra of perylene pigments, J. Am. Chem. Soc. 116 (1994) 9684–9691.

[29] A.E. Clark, C. Qin, A.D. Li, Beyond exciton theory: a time-dependent DFT and Franck − Condon study of perylene diimide and its chromophoric dimer, J. Am. Chem. Soc. 129 (2007) 7586–7595.

[30] X.Q. Li, X. Zhang, S. Ghosh, F. Würthner, Highly fluorescent lyotropic mesophases and organogels based on J-aggregates of core-twisted perylene bisimide dyes, Chem. Eur. J. 14 (2008) 8074–8078.

[31] H. Wu, L. Xue, Y. Shi, Y. Chen, X. Li, Organogels based on J- and H-type aggregates of amphiphilic perylenetetracarboxylic diimides, Langmuir 27 (2011) 3074–3082.

[32] S. Ghosh, X.Q. Li, V. Stepanenko, F. Würthner, Control of H-and J-type π stacking by peripheral Alkyl chains and self-sorting phenomena in perylene bisimide homo-and heteroaggregates, Chem. Eur. J. 14 (2008) 11343–11357.

[33] D. Görl, X. Zhang, F. Würthner, Molecular assemblies of perylene bisimide dyes in water, Angew. Chem. Int. Ed. 51 (2012) 6328–6348.

[34] A. Datar, K. Balakrishnan, L. Zang, One-dimensional self-assembly of a water soluble perylene diimide molecule by pH triggered hydrogelation, Chem. Commun. 49 (2013) 6894–6896.

[35] K. Balakrishnan, A. Datar, T. Naddo, J. Huang, R. Oitker, M. Yen, J. Zhao, L. Zang, Effect of side-chain substituents on self-assembly of perylene diimide molecules: morphology control, J. Am. Chem. Soc. 128 (2006) 7390–7398.

[36] A.L. Briseno, S.C. Mannsfeld, C. Reese, J.M. Hancock, Y. Xiong, S.A. Jenekhe, Z. Bao, Y. Xia, Perylenediimide nanowires and their use in fabricating field-effect transistors and complementary inverters, Nano Lett. 7 (2007) 2847–2853.

[37] J.M. Giaimo, J.V. Lockard, L.E. Sinks, A.M. Scott, T.M. Wilson, M.R. Wasielewski, Excited singlet states of covalently bound, cofacial dimers and trimers of perylene-3, 4:9, 10-bis (dicarboximide) s, J. Phys. Chem. A. 112 (2008) 2322–2330.

[38] K. Balakrishnan, A. Datar, R. Oitker, H. Chen, J. Zuo, L. Zang, Nanobelt self-assembly from an organic n-type semiconductor: propoxyethyl-PTCDI, J. Am. Chem. Soc. 127 (2005) 10496–10497.

[39] Z. Chen, V. Stepanenko, V. Dehm, P. Prins, L.D. Siebbeles, J. Seibt, P. Marquetand, V. Engel, F. Würthner, Photoluminescence and conductivity of self-assembled π–π stacks of perylene bisimide dyes, Chem. Eur. J. 13 (2007) 436–449.

[40] T.E. Kaiser, H. Wang, V. Stepanenko, F. Würthner, Supramolecular construction of fluorescent J-aggregates based on hydrogen-bonded perylene dyes, Angew. Chem. Int. Ed. 46 (2007) 5541–5544.

[41] F. Wuerthner, C. Bauer, V. Stepanenko, S. Yagai, A black perylene bisimide super gelator with an unexpected J-type absorption band, Adv. Mater. 20 (2008) 1695–1698.

[42] S. Yagai, T. Seki, T. Karatsu, A. Kitamura, F. Würthner, Transformation from H-to J-aggregated perylene bisimide dyes by complexation with cyanurates, Angew. Chem. Int. Ed. 47 (2008) 3367–3371.

[43] Y. Che, A. Datar, K. Balakrishnan, L. Zang, Ultralong nanobelts self-assembled from an asymmetric perylene tetracarboxylic diimide, J. Am. Chem. Soc. 129 (2007) 7234–7235.

[44] R. Singh, E. Giussani, M.M. Mróz, F. Di Fonzo, D. Fazzi, J. Cabanillas-González, L. Oldridge, N. Vaenas, A.G. Kontos, P. Falaras, On the role of aggregation effects in the performance of perylene-diimide based solar cells, Org. Electron. 15 (2014) 1347–1361.

[45] D. Chen, Z. Wang, T. Ren, H. Ding, W. Yao, R. Zong, Y. Zhu, Influence of defects on the photocatalytic activity of ZnO, J. Phys. Chem. C. 118 (2014) 15300–15307.

[46] R.W. Redmond, J.N. Gamlin, A compilation of singlet oxygen yields from biologically relevant molecules, Photochem. Photobiol. 70 (1999) 391–475.

[47] H. Wang, X. Yang, W. Shao, S. Chen, J. Xie, X. Zhang, J. Wang, Y. Xie, Ultrathin black phosphorus nanosheets for efficient singlet oxygen generation, J. Am. Chem. Soc. 137 (2015) 11376–11382.

[48] J. Di, J. Xia, M. Ji, B. Wang, S. Yin, Q. Zhang, Z. Chen, H. Li, Carbon quantum dots modified BiOCl ultrathin nanosheets with enhanced molecular oxygen activation ability for broad spectrum photocatalytic properties and mechanism insight, ACS Appl. Mater. Inter. 7 (2015) 20111–20123.

[49] Q. Hao, R. Wang, H. Lu, C. Ma, D. Chen, W. Yao, Y. Zhu, One-pot synthesis of C/Bi/Bi2O3 composite with enhanced photocatalytic activity, Appl. Catal. B: Environ. 219 (2017) 63–72.

[50] P. Qiu, C. Xu, H. Chen, F. Jiang, X. Wang, R. Lu, X. Zhang, One step synthesis of oxygen doped porous graphitic carbon nitride with remarkable improvement of photo-oxidation activity: Role of oxygen on visible light photocatalytic activity, Appl. Catal. B: Environ. 206 (2017) 319–327.

[51] G. Yang, D. Chen, H. Ding, J. Feng, J.Z. Zhang, Y. Zhu, S. Hamid, D.W. Bahnemann, Well-designed 3D ZnIn2S4 nanosheets/TiO2 nanobelts as direct Z-scheme photocatalysts for CO2 photoreduction into renewable hydrocarbon fuel with high

efficiency, Appl. Catal. B: Environ. 219 (2017) 611–618.

[52] O. Legrini, E. Oliveros, A. Braun, Photochemical processes for water treatment, Chem. Rev. 93 (1993) 671–698.

[53] M.R. Hoffmann, S.T. Martin, W. Choi, D.W. Bahnemann, Environmental applications of semiconductor photocatalysis, Chem. Rev. 95 (1995) 69–96.

[54] C. Chen, W. Ma, J. Zhao, Semiconductor-mediated photodegradation of pollutants under visible-light irradiation, Chem. Soc. Rev. 39 (2010) 4206–4219.

[55] R. Shi, Y. Cao, Y. Bao, Y. Zhao, G.I. Waterhouse, Z. Fang, L.Z. Wu, C.H. Tung, Y. Yin, T. Zhang, Self-assembled Au/CdSe nanocrystal clusters for plasmon-mediated

photocatalytic hydrogen evolution, Adv. Mater. 29 (2017).

[56] Y. Zhao, B. Zhao, J. Liu, G. Chen, R. Gao, S. Yao, M. Li, Q. Zhang, L. Gu, J. Xie, Oxide-modified nickel photocatalysts for the production of hydrocarbons in visible light, Angew. Chem. Int. Ed. 55 (2016) 4215–4219.

[57] J. Rengifo-Herrera, K. Pierzchała, A. Sienkiewicz, L. Forro, J. Kiwi, C. Pulgarin, Abatement of organics and Escherichia coli by N, S co-doped TiO 2 under UV and visible light. Implications of the formation of singlet oxygen (1O2) under visible light, Appl. Catal. B: Environ. 88 (2009) 398–406.